

Neural Error Mitigation of Near-Term Quantum Simulations

Elizabeth R. Bennewitz,^{1,2,3,*} Florian Hopfmueller,^{1,2,3,*}

Bohdan Kulchytskyy,¹ Juan Carrasquilla,^{4,2} and Pooya Ronagh^{5,2,3,6,†}

¹*1QB Information Technologies (1QBit), Waterloo, ON, Canada*

²*Department of Physics & Astronomy, University of Waterloo, Waterloo, ON, Canada*

³*Perimeter Institute for Theoretical Physics, Waterloo, ON, Canada*

⁴*Vector Institute, MaRS Centre, Toronto, ON, Canada*

⁵*Institute for Quantum Computing, University of Waterloo, Waterloo, ON, Canada*

⁶*1QBit, Vancouver, BC, Canada*

(Dated: January 31, 2023)

Near-term quantum computers provide a promising platform for finding ground states of quantum systems, which is an essential task in physics, chemistry, and materials science. Near-term approaches, however, are constrained by the effects of noise as well as the limited resources of near-term quantum hardware. We introduce *neural error mitigation*, which uses neural networks to improve estimates of ground states and ground-state observables obtained using near-term quantum simulations. To demonstrate our method’s broad applicability, we employ neural error mitigation to find the ground states of the H₂ and LiH molecular Hamiltonians, as well as the lattice Schwinger model, prepared via the variational quantum eigensolver (VQE). Our results show that neural error mitigation improves numerical and experimental VQE computations to yield low energy errors, high fidelities, and accurate estimations of more-complex observables like order parameters and entanglement entropy, without requiring additional quantum resources. Furthermore, neural error mitigation is agnostic with respect to the quantum state preparation algorithm used, the quantum hardware it is implemented on, and the particular noise channel affecting the experiment, contributing to its versatility as a tool for quantum simulation.

I. INTRODUCTION

Since the early twentieth century, scientists have been developing comprehensive theories that describe the behaviour of quantum mechanical systems. However, the computational cost required to study these systems often exceeds the capabilities of current scientific computing methods and hardware. Consequently, computational infeasibility remains a roadblock for the practical application of those theories to problems of scientific and technological importance.

The simulation of quantum systems on quantum computers, referred to in this paper as quantum simulation, shows promise toward overcoming these roadblocks, and has been a foundational driving force behind the conception and creation of quantum computers [1–4]. In particular, the quantum simulation of ground and steady states of quantum many-body systems beyond the capabilities of classical computers is expected to significantly impact nuclear physics, particle physics, quantum gravity, condensed matter physics, quantum chemistry, and materials science [5–8]. The capabilities of current and near-term quantum computers continue to be constrained by limitations, such as the number of qubits and the effects of noise. Quantum error correction (QEC) techniques can eliminate errors that result from noise, providing a path toward fault-tolerant quantum compu-

tation. However, in practice, implementing QEC imposes a large overhead in terms of both the required number of qubits and low error rates, both of which remain beyond the capabilities of current and near-term devices.

Before fault-tolerant quantum simulations [9] can be realized, modern variational algorithms significantly alleviate the demand on quantum hardware and exploit the capabilities of noisy intermediate-scale quantum (NISQ) devices [10, 11]. A prominent example is the variational quantum eigensolver (VQE) [12], a hybrid quantum–classical algorithm that iteratively approximates the lowest-energy eigenvalues of a target Hamiltonian through the variational optimization of a family of parameterized quantum circuits. This, and other variational algorithms, has emerged as a leading strategy toward achieving a quantum advantage using near-term devices and accelerating progress in multiple scientific and technological fields [13].

The experimental implementation of variational quantum algorithms remains a challenge for many scientific problems, as NISQ devices suffer from various sources of noise and imperfection. To alleviate these issues, several methods for quantum error mitigation (QEM) have been proposed and experimentally validated that improve quantum computations in the absence of the quantum resources required for QEC [14]. For a review of current QEM techniques, we refer the reader to Ref. [13] and the material cited therein. In general, these methods use specific information about the noise channels that affect a quantum computation, the hardware implementation, or the quantum algorithms themselves. Examples include the implicit characterization of noise models and how

* E. R. B and F. H. have contributed equally to this work.

† Corresponding author: pooya.ronagh@1qbit.com

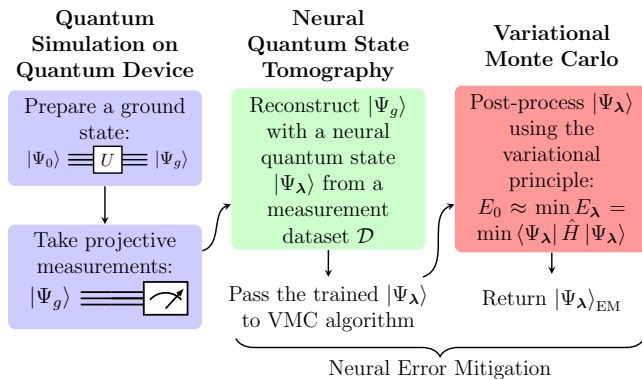


FIG. 1: **Neural error mitigation procedure** | First, an approximate ground state $|\Psi_g\rangle$ is prepared on a quantum computer from which simple projective measurements are taken (left column). This measurement dataset, \mathcal{D} , is then used to reconstruct the final state $|\Psi_g\rangle$ with a neural quantum state $|\Psi_\lambda\rangle$ using neural quantum state tomography (middle column). Then, the neural network ansatz is post-processed using variational Monte Carlo to mitigate errors in the ground-state representation (right column).

they affect estimates of the desired observables, specific knowledge of the state subspaces in which the prepared quantum state ought to reside, and the characterization and mitigation of the sources of noise on individual components of the quantum computation such as single- and two-qubit gate errors, as well as state preparation and measurement (SPAM) errors.

Machine learning techniques, which have recently been repurposed as tools for tackling complex problems in quantum many-body physics and quantum information processing [15, 16], provide an alternative route to QEM. Here we introduce a QEM strategy named *neural error mitigation* (NEM), which uses neural networks to mitigate errors in the approximate preparation of the quantum ground state of a Hamiltonian.

The NEM algorithm, summarized in Fig. 1, is composed of two steps. First, we perform neural quantum state tomography (NQST) to train a neural quantum state (NQS) ansatz to represent the approximate ground state prepared by a noisy quantum device, using experimentally accessible measurements. Inspired by traditional quantum state tomography (QST), NQST is a data-driven machine learning approach to QST that uses a limited number of measurements to efficiently reconstruct complex quantum states [8]. We then apply the variational Monte Carlo algorithm (VMC) on the same neural quantum state ansatz (which we call the NEM ansatz) to improve the representation of the unknown ground state. In the spirit of VQE, VMC approximates the ground state of a Hamiltonian based on a classical variational ansatz [18], in this case a NQS ansatz.

In this paper, we use an autoregressive generative neural network as our NEM ansatz. In particular, we use the Transformer [1] architecture, and show that this model performs well as a neural quantum state. Due to its capability to model long-range temporal and spatial correlations, this architecture has led to many state-of-the-art

results in natural language and image processing, and has the potential to model long-range quantum correlations. We refer the reader to the Methods section and Supplementary Information for a complete description of NQS, NQST, VMC, and the Transformer neural network.

Neural error mitigation has several advantages compared to other error mitigation techniques. Firstly, it has a low experimental overhead; it requires only a set of simple experimentally feasible measurements to learn the properties of the noisy quantum state prepared by VQE. Consequently, the overhead of error mitigation in NEM is shifted from quantum resources (i.e., performing additional quantum experiments and measurements) to classical computing resources for machine learning. In particular, we note that the primary cost of NEM is in performing VMC until convergence. Another advantage of NEM is that it is agnostic with respect to the quantum simulation algorithm, the device it is implemented on, and the particular noise channel affecting the quantum simulation. As a result, it can also be combined with other QEM techniques [20, 21], and can be applied to either analog quantum simulation or digital quantum circuits [22, 23].

Neural error mitigation also alleviates the low measurement precision that arises when estimating quantum observables using near-term quantum devices. This is particularly important in quantum simulations, where making accurate estimations of quantum observables is essential for practical applications. Neural error mitigation intrinsically resolves the low measurement precision at each step of the algorithm. During the first step, NQST improves the variance of observable estimates at the cost of introducing a small estimation bias [24]. This bias, as well as the remaining variance, is further reduced by training the NEM ansatz using VMC, which results in a zero-variance expectation value for energy estimates once the ground state has been reached [25].

II. RESULTS

A. Quantum Chemistry Results

Accurately simulating a molecule’s electron correlations is an integral step in characterizing the chemical properties of the molecule. This problem, known as the electronic structure problem, involves finding the ground-state wavefunction and energy of many-body interacting fermionic molecular Hamiltonians. Achieving an absolute energy error corresponding to chemical accuracy (1 kcal/mol \approx 0.0016 hartrees), the threshold for accurately estimating room-temperature chemical reaction rates, is essential to applications in drug discovery and materials science [7].

We demonstrate the application of NEM to the estimation of molecular ground states prepared using a VQE algorithm and show that our method improves the results up to chemical accuracy or better for the H_2 and LiH

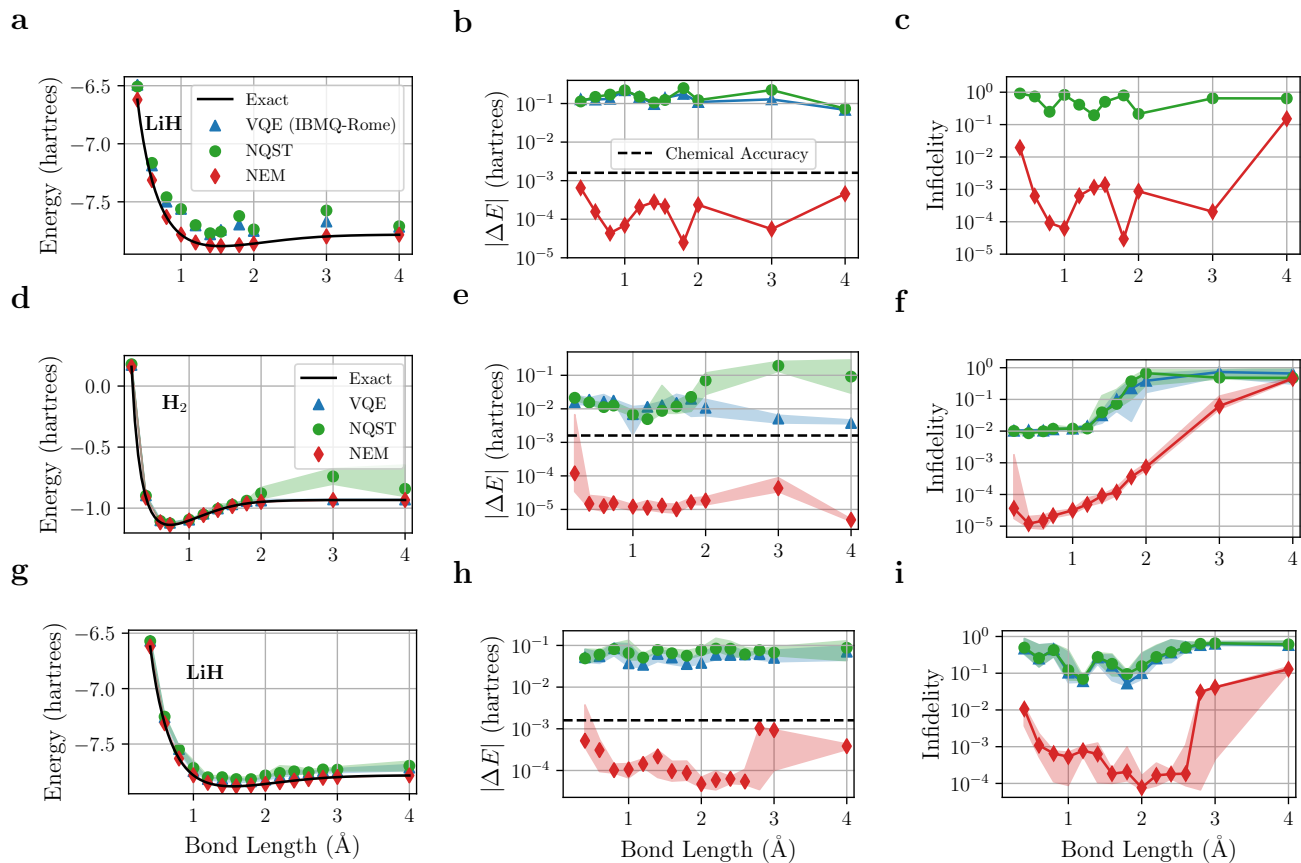


FIG. 2: **Neural error mitigated experimental and numerical results for molecular Hamiltonians** | Neural error mitigation results for energy, energy error, and infidelity for the ground states of LiH and H_2 prepared using a hardware-efficient variational quantum circuit. Each panel contains information about the prepared quantum states (blue triangles), neural quantum states trained using neural quantum state tomography (green circles), the final neural error mitigated states (red diamonds), and, where appropriate, the exact results (solid black line). The top row (a - c) shows results for the LiH ground state prepared experimentally using IBM’s five-qubit device, IBMQ-Rome. The middle row (d - f) and bottom row (g - i) show the performance of neural error mitigation for numerically prepared H_2 and LiH ground states, respectively. Results are shown for the median performance over 10 noisy numerical simulations per bond length, and the shaded region is the interquartile range. For our ten data points, the interquartile range includes the middle six and excludes the best two and worst two in order to indicate the typical performance of the method. Error mitigated results extend both the experimentally and numerically prepared VQE states to chemical accuracy and low infidelities for all bond lengths of LiH and H_2 . Chemical accuracy is shown at 0.0016 hartrees (dashed black line).

molecules (see Fig. 2 for experimental and numerical results). We map the H_2 and LiH molecular Hamiltonians computed in the STO-3G basis to qubit Hamiltonians with $N = 2$ and $N = 4$ qubits, respectively [7]. The prepared quantum state is the hardware-efficient variational quantum circuit composed of single-qubit Euler rotation gates and two-qubit CNOT entangling gates native to superconducting hardware [7]. For both H_2 and LiH, we construct a variational circuit with a single entangling layer, giving a variational circuit with 10 and 20 parameters, respectively. More details can be found in the Methods section.

We highlight the performance of NEM on the experimental preparation of the ground states of LiH at different bond lengths using IBM’s five-qubit chip, IBMQ-Rome. We map the four-qubit LiH problem to the four linearly connected qubits on IBMQ-Rome that have the lowest average single- and two-qubit gate errors. During optimization, we perform 250 iterations of simultaneous perturbation stochastic approximation (SPSA) optimiza-

tion to obtain the final prepared quantum state. Neural error mitigation improves the results of VQE to chemical accuracy or better for all bond lengths, and achieves infidelities, given by $1 - |\langle \Psi | \Psi_0 \rangle|^2$, of 10^{-3} for most bond lengths (shown in top row of Fig. 2). On average, NEM achieves an improvement of three orders of magnitude on energy estimation and two orders of magnitude on infidelity. We provide further details about the reconstruction quality in the Supplementary Information, including an analysis of the reconstructed neural quantum state.

Additionally, we illustrate the results of applying NEM on the ground states of H_2 and LiH prepared using classically simulated VQE with a depolarizing noise channel (shown in bottom two rows of Fig. 2). We simulate VQE with a single-qubit depolarizing error probability of 0.001 and two-qubit depolarizing error probability of 0.01. At each bond length, we generate 10 VQE simulations and report the NEM results. Notably, the median performance of NEM improves the ground-state estimation of H_2 and LiH to chemical accuracy and low infi-

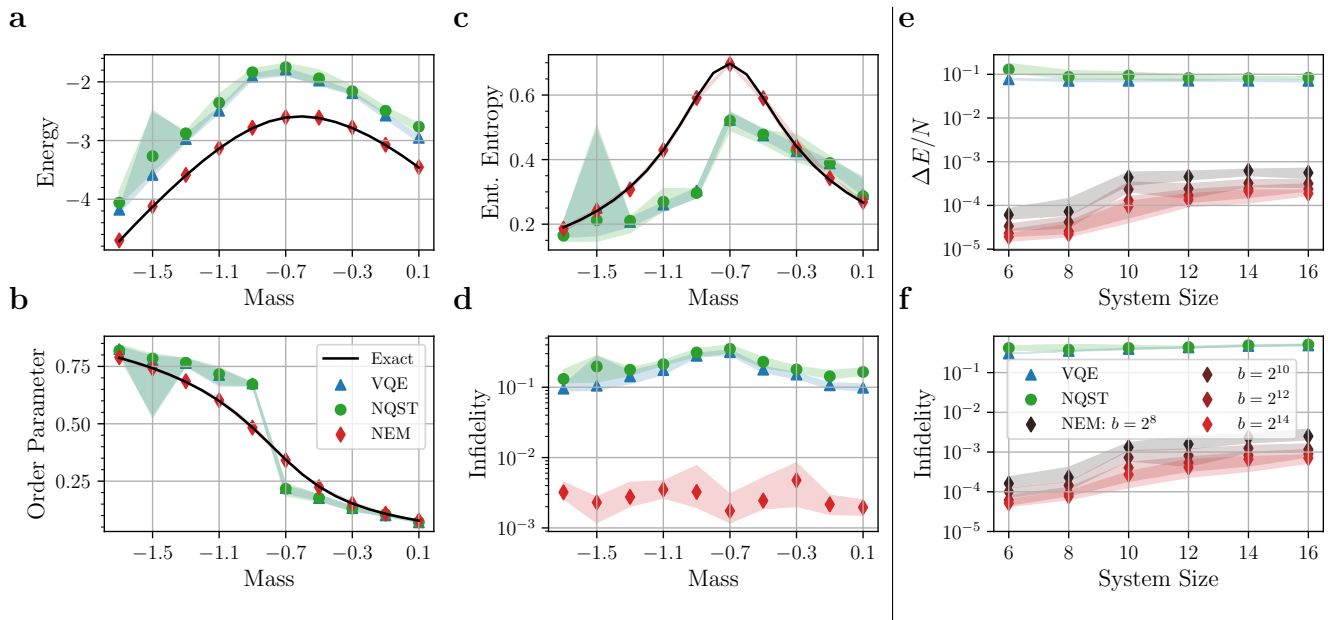


FIG. 3: **Performance of neural error mitigation applied to ground states of the lattice Schwinger model** | *Left*: Estimates for (a) the ground state energy, (b) order parameter, (c) entanglement entropy between the first three and remaining five sites, and (d) infidelity to the exact ground state, for the $N = 8$ site model. Each panel contains results for the quantum states prepared using VQE simulated with a depolarizing noise channel (blue triangles), neural quantum states trained using neural quantum state tomography (green circles), the final neural error mitigated neural quantum states (red diamonds), and, where applicable, exact results (solid black lines). While the qualitative behaviour of the entanglement entropy and the order parameter across the phase transition are not modelled well by VQE or NQST, applying NEM consistently improves the estimates of all observables to low errors and low infidelities. *Right*: Results of the scaling study of NEM at the phase transition ($m = -0.7$) are shown for (e) the energy error per site and (f) infidelity, as a function of system size. The performance of VQE without noise (blue triangles) shows an approximately constant energy error per site with infidelities that become slightly worse as system size increases. Across all sizes, applying NEM (red diamonds) improves VQE performance by two to four orders of magnitude, even when using a small VMC batch size of $b = 2^8$, which is the number of samples used to estimate the energy's gradient in one iteration of VMC. In all panels (left and right), median values over 10 runs are shown, and the shaded region is the interquartile range.

delities for all bond lengths. The increased infidelity for bond lengths larger than 2\AA , as shown in the infidelity plots of Fig. 2, can be explained by the decreasing energy gap between the ground state and the first excited state. When the energy gap is small, it becomes more difficult for methods that optimize the energy, like VQE and VMC, to isolate the ground-state representation.

B. Lattice Schwinger Results

We next apply our method to the ground state of the lattice Schwinger model, which is a prototypical abelian lattice gauge theory, and a toy model for quantum electrodynamics in one spatial dimension. Multiple experiments have been proposed that use quantum devices to explore the properties of this model [27–30]. In this paper, we consider the experiment where a trapped-ion analog quantum simulator is used to variationally prepare the ground state of the lattice Schwinger model using alternating entangling operations, e^{itH_E} , which act on all qubits simultaneously, and single qubit rotations [27].

After using a Jordan–Wigner transformation to map the fermionic degrees of freedom of the theory to qubits, the lattice Schwinger Hamiltonian takes the following [27]

form:

$$\hat{H} = \frac{w}{2} \sum_{j=1}^{N-1} (\hat{X}_j \hat{X}_{j+1} + \hat{Y}_j \hat{Y}_{j+1}) + \frac{m}{2} \sum_{j=1}^N (-1)^j \hat{Z}_j + \bar{g} \sum_{j=1}^N \hat{L}_j^2. \quad (1)$$

The first term describes the creation and annihilation of electron–positron pairs and contains an overall energy scale, w . The second term contains the bare electron mass m , and the third term contains \bar{g}_j , which is the coupling strength to the electric field \hat{L}_j . Solving for the electric field in one spatial dimension gives $\hat{L}_j = \epsilon_0 - \frac{1}{2} \sum_{\ell=1}^j (\hat{Z}_\ell + (-1)^\ell \hat{I})$, where ϵ_0 is an integration constant. Given that the quantum fields at one spatial lattice point are encoded into a pair of qubits, the total number of sites N must be even. We set $w = 1, \bar{g} = 1$, and $\epsilon_0 = 0$ such that the only remaining parameter is the mass m . The ground state of the system for $m \rightarrow +\infty$ describes a vacuum with no electron–positron pairs and for $m \rightarrow -\infty$ describes a large number of electron–positron pairs. In the thermodynamic limit, the model exhibits a second-order phase transition at $m \approx -0.7$, which can be detected using the order parameter $\langle \mathcal{O} \rangle = \frac{1}{2N(N-1)} \sum_{i,j>i} \langle (1 + (-1)^i \hat{Z}_i)(1 + (-1)^j \hat{Z}_j) \rangle$. The model possesses discrete symmetries, which inform

the choice of a variational quantum circuit with a manageable number of parameters, but, in order to demonstrate the general applicability of NEM, we do not enforce these symmetries on the neural quantum state.

We demonstrate the performance of neural error mitigation by applying it to the approximate ground state of the lattice Schwinger model obtained by numerically simulating a VQE algorithm for $N = 8$ sites, with single-qubit depolarizing noise with probability $\lambda = 0.001$ applied after each rotation and entangling operation. As shown in Fig. 3a through Fig. 3d, the simple VQE scheme we employ exhibits median infidelities between 0.10 and 0.31, with worse performance closer to the phase transition around $m = -0.7$. While the qualitative behaviour of the ground-state energy as a function of the mass is modelled approximately by VQE, the qualitative behaviour of other physical properties is not reproduced well, limiting the utility of our VQE results for studying the phase transition. This includes the order parameter, and the Renyi entanglement entropy S_2 of a partition of the system, which is a broadly used, experimentally accessible quantity [31, 32] expressing the amount of correlation present in the quantum state.

The properties of the NEM state show a substantial improvement over VQE. The NEM state reaches absolute energy errors on the order of 10^{-2} , and infidelities approaching 10^{-3} . Importantly, after applying NEM, the physical properties estimated by the state accurately follow their exact values. The ability to obtain precise estimations of these physical properties can be explained by the accurate representation of the ground-state wavefunction captured by the NEM neural quantum state. Further details about the reconstruction quality of each component are covered in the Supplementary Information, including a thorough analysis of the NEM neural quantum state.

To gather evidence that the performance of NEM scales well to larger near-term experiments on quantum devices, we study the behaviour of NEM as a function of system size for the lattice Schwinger model. For computational efficiency, the scaling study uses a modified VQE implementation without noise (see Fig. 3e and Fig. 3f) as compared to the simulated trapped-ion experiment (see Fig. 3a through Fig. 3d). For more details on the modified circuit, we refer the reader to the Methods section. The VQE algorithm is simulated on a classical computer for system sizes up to $N = 16$, and NEM is applied to the resulting states. The results in Fig. 3e and Fig. 3f show that NEM improves upon the VQE results by two to four orders of magnitude, even for large system sizes, using modest classical resources for the estimation of energy gradients in VMC.

III. DISCUSSION

The error mitigation strategy developed here demonstrates significant improvements to the estimations of

ground states and ground-state observables obtained from two example classes of near-term quantum simulations, independent of the quantum device and noise channels. Additionally, we show that NEM exhibits the potential to scale well for such quantum experiments. Given its low quantum overhead, NEM can be a powerful asset for the error mitigation of near-term quantum simulations.

An advantage of using techniques based on neural quantum states for the task of quantum error mitigation is the ability to approximate complex wavefunctions from simple experimental measurements. In the process of improving the energy estimation performed by VQE, NEM reconstructs and improves the ground-state wavefunction itself as a neural quantum state. The accurate final representation of the ground-state wavefunction is the reason why NEM is able to accurately reconstruct and improve estimations of complex observables like energy, order parameters, and entanglement entropy without imposing additional quantum resources.

By combining VQE, which uses a parametric quantum circuit as an ansatz, and NQST and VMC, which use neural networks as an ansatz, NEM brings together two families of parametric quantum states and three optimization problems over their loss landscapes [33–35]. Our work raises the question as to the nature of the relationships between these families of states, their loss landscapes, and quantum advantage. Examining these relationships offers a new way to investigate the potential of NISQ algorithms in seeking a quantum advantage. This may lead to a better delineation between classically tractable simulations of quantum systems and those that require quantum resources.

IV. METHODS

A. Neural Quantum State

Our neural quantum state is based on the Transformer [1], an architecture originally developed to process sequences that have temporal and spatial correlations, such as written languages. Compared to previous architectures for sequence models such as the long short-term memory (LSTM) neural network [36], the Transformer excels at modelling long-range correlations, and has thus become very popular in machine learning. Within the quantum many-body machine learning community, there has been a lot of work using autoregressive neural networks as neural quantum states [37, 38]. Recently, the Transformer has been adapted as an autoregressive generative neural quantum state [39].

We represent the quantum state $|\psi\rangle$ with a Transformer neural network that takes as input a bitstring $s = (s_1, \dots, s_N) \in \{0, 1\}^N$, describing a computational basis state $|s\rangle$, where N is the number of qubits. The neural network outputs two numbers $(p_{\vec{\lambda}}(s), \varphi_{\vec{\lambda}}(s))$ parameterized by the neural network weights $\vec{\lambda}$, which form

the complex amplitude $\langle s|\psi_{\vec{\lambda}}\rangle$ given by

$$\langle s|\psi_{\vec{\lambda}}\rangle = \sqrt{p_{\vec{\lambda}}(s)}e^{i\varphi_{\vec{\lambda}}(s)}. \quad (2)$$

Here, $p_{\vec{\lambda}}(s)$ is a normalized probability distribution, which automatically normalizes the quantum state. The autoregressive property of the model allows for efficient sampling from the Born distribution of $|\psi_{\vec{\lambda}}\rangle$ in the computational basis. More details may be found in the Supplementary Information.

The exact ground state amplitudes of both the quantum chemistry models and the lattice Schwinger model are real, that is, $\varphi(s) \in \{0, \pi\}$, and the signs of the lattice Schwinger model ground-state amplitudes follow a simple sign rule. However, to show the general applicability of our method, we do not enforce any of these conditions in our neural quantum states.

B. Neural Quantum State Tomography

In neural quantum state tomography [8], a neural network is trained to represent the state of a quantum device using samples from that state in various Pauli bases (i.e., after performing various post-rotations). Neural quantum state tomography proceeds by iteratively adjusting the NQS parameters to maximize the likelihood that NQS assigns to the samples.

A sample $s \in \{0, 1\}^N$ in a Pauli basis $B = P_1 P_2 \cdots P_N$, with $P_i \in \{X, Y, Z\}$, is the unique simultaneous eigenstate of the single qubit Pauli operators P_i , with eigenvalues determined by the entries of s . We denote such a state by $|s, B\rangle$. The likelihood of the sample (s, B) according to the neural quantum state $|\psi_{\vec{\lambda}}\rangle$ is given by

$$\begin{aligned} p_{\vec{\lambda}}(s, B) &= |\langle s, B|\psi_{\vec{\lambda}}\rangle|^2 \\ &= \left| \sum_{\substack{t \in \{0, 1\}^N \\ \langle s, B|t\rangle \neq 0}} \langle s, B|t\rangle \langle t|\psi_{\vec{\lambda}}\rangle \right|^2. \end{aligned} \quad (3)$$

Here, we sum over the computational basis states $|t\rangle$ that have a non-zero overlap with the given sample $|s, B\rangle$. For a single sample $|s, B\rangle$, the number of these states $|t\rangle$ is 2^K , where K is the number of positions i where $P_i \neq Z$. Therefore, the computational cost of a single iteration of tomography training is proportional to 2^K . To constrain this computational cost, we use projective measurements in *almost-diagonal* Pauli bases (i.e., Pauli bases B with low numbers of X or Y terms).

In order to learn the quantum state from a set of measurements \mathcal{D} , the objective function minimized during NQST is an approximation of the cross entropy averaged over the set of bases \mathcal{B} from which samples were drawn [24], and is given by

$$L_{\vec{\lambda}} = -\frac{1}{|\mathcal{B}|} \sum_{B \in \mathcal{B}} \sum_{s \in \{0, 1\}^N} p_{\text{VQE}}(s, B) \ln p_{\vec{\lambda}}(s, B). \quad (4)$$

Here, $p_{\text{VQE}}(s, B)$ is the exact, unknown likelihood of measuring $|s, B\rangle$ from the VQE state. The cross entropy achieves its minimum in $\vec{\lambda}$ if $p_{\text{VQE}}(s, B) = p_{\vec{\lambda}}(s, B)$. As commonly done in unsupervised learning, the cross entropy is approximated using the set \mathcal{D} of the measured samples $|s, B\rangle$, which is further partitioned into training and validation subsets $\mathcal{D}_{T, V}$. The loss function used in training is

$$L_{\vec{\lambda}} \approx -\frac{1}{|\mathcal{D}_T|} \sum_{|s, B\rangle \in \mathcal{D}_T} \ln p_{\vec{\lambda}}(s, B). \quad (5)$$

The training is performed using stochastic gradient descent (SGD) with the Adam [40] optimizer.

C. Variational Monte Carlo and Regularization

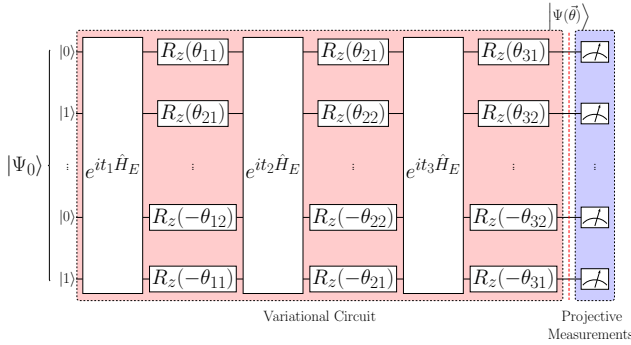
Variational Monte Carlo is a method that adjusts the parameters of a (classical) variational wavefunction ansatz in order to approximate the ground state of a given Hamiltonian. The method usually proceeds by gradient-based optimization of the energy, where the energy and its partial derivatives with respect to the ansatz parameters are estimated using Monte Carlo samples drawn from the classical variational wavefunction. As detailed in the Supplementary Information, the autoregressive property of our neural network wavefunction allows for efficient sampling of the learned probability distribution. This leads to more efficient VMC training compared to models such as restricted Boltzmann machines (RBM) [10, 41], where samples have to be obtained using Markov chain Monte Carlo.

Many implementations of VMC use second-order methods involving the Hessian of the energy [43], or other update rules such as stochastic reconfiguration [41], to update the parameters. These methods tend to be computationally expensive for models with large numbers of parameters. Instead, we use SGD via the Adam optimizer, leading to an update-step cost that is linear in the number of parameters, and hence scales more favourably for larger models.

We find it necessary to add a regularization term to the VMC objective in the early stages of VMC optimization. Without it, the magnitudes of the amplitudes of some computational basis states decrease to almost zero over the course of training, even for computational basis states which have a non-zero overlap with the true ground state. It has been previously noted [10] that the VMC algorithm has difficulty finding the ground state of molecular Hamiltonians because they have sharply peaked amplitudes in a sparse subset of the computational basis states. The regularization term is designed to increase very small amplitudes. It maximizes the L_1 norm of the state, thereby discouraging sparsity. This is in contrast to the common usage of L_1 regularization in machine learning and optimization where the L_1

norm is minimized to encourage sparsity in sparse optimization tasks. We expect this technique to be useful for systems where the ground state has a large overlap with one or a few computational basis states. For example, ground states of electronic structure problems have a large overlap with the Hartree–Fock state and the lattice Schwinger ground states have a large overlap with the ground states for $m \rightarrow \pm\infty$. This regularization technique allows the NQS to capture the subdominant amplitudes, rather than collapsing onto the dominant computational basis state early in the training process. The L_1 norm can be estimated in a tractable manner because we use an autoregressive, generative neural network as our neural quantum state, which allows for the exact sampling of the learned probability distribution and is automatically normalized. More details on the regularization term and the VMC algorithm can be found in the Supplementary Information.

a



b

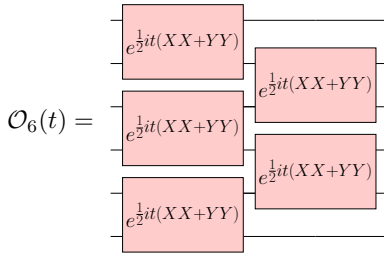


FIG. 4: **VQE ansatz circuits for the lattice Schwinger model** | (a) Variational quantum circuit used to prepare the approximate ground state of the lattice Schwinger model, using VQE simulated classically. The input state $|\Psi_0\rangle$ is $|01\dots 01\rangle$ ($|10\dots 10\rangle$) for $m \geq -0.7$ ($m < -0.7$). (b) For the results shown in Fig. 3e and Fig. 3f, the entangling layers of (a) are replaced with \mathcal{O}_N for N sites. The layers of single-qubit gates are left unchanged.

D. The VQE Implementation for Quantum Chemistry

We use the variational quantum circuit in Eq. (6) for the electronic structure problem in quantum chemistry. This ansatz was designed for the hardware capabilities of current superconducting quantum processors [7]. We

use this circuit for both our numerical simulations with a depolarizing noise channel, as well as to perform experiments on a five-qubit superconducting quantum processor (Fig. 2).

The H_2 and LiH molecular Hamiltonians are mapped to qubit Hamiltonians with $N = 2$ and $N = 4$ qubits, respectively [7]. In particular, we map the second-quantized fermionic Hamiltonian for H_2 to its qubit Hamiltonian using the Bravyi–Kitaev transformation [44] while the LiH Hamiltonian is transformed using the parity transformation [44, 45]. In each case, two qubits associated with the spin-parity symmetries of the model are removed to obtain final qubit Hamiltonians [46].

The hardware-efficient variational quantum circuit is composed of single-qubit rotations and two-qubit entangling gates native to superconducting hardware. The variational circuit,

$$|\psi(\vec{\theta})\rangle = \prod_{l=1}^d \left(\prod_{q=1}^N [U_{\text{EUR}}^{q,l}(\vec{\theta})] \times U_{\text{ENT}} \right) \times \prod_{q=1}^N [U^{q,0}(\vec{\theta})] |00\dots 0\rangle, \quad (6)$$

for N qubits consists of d CNOT entangling layers alternating with $N(d+1)$ single-qubit Euler rotations, given by $U(\vec{\theta}) = R_Z(\theta_1)R_X(\theta_2)R_Z(\theta_3)$. In the first rotation layer, $U^{q,0}(\vec{\theta})$, the first set of Z rotations is not implemented, reducing the number of circuit parameters. Within each entangling layer, we apply CNOT gates on pairs of linearly connected qubits. The variational circuit has $p = N(3d+2)$ independent parameters. For both H_2 and LiH , we construct a variational circuit with $d = 1$ entangling layers giving 10 and 20 parameters, respectively.

The variational circuit is then optimized using Qiskit’s implementation of simultaneous perturbation stochastic approximation (SPSA) [47] for 250 iterations to obtain an estimation for the ground-state energy of H_2 and LiH . Each SPSA iteration requires two energy evaluations. In order to reduce the sampling overhead during the energy estimations, Pauli terms in each Hamiltonian are grouped according to their common tensor product basis [7], requiring only two and 25 circuits with unique post-rotations for H_2 and LiH , respectively, to estimate the energy.

In order to perform NQST, we collect almost-diagonal measurement samples from the final noisy state prepared by the variational procedure. In this case, the nearly diagonal samples are taken in the following bases: in the all- Z basis, in the N bases with one X (and Z elsewhere), and in the $(N(N-1)/2)$ bases with two X s (and Z elsewhere).

E. The VQE Implementation for the Lattice Schwinger Model

Our variational quantum circuit for the lattice Schwinger model closely follows the variational circuit implementation on a trapped-ion analog quantum simulator [27] that approximately preserves the symmetries of the lattice Schwinger model.

The quantum state is first prepared in $|01\dots 01\rangle$ for $m \geq 0.7$ and $|10\dots 10\rangle$ for $m < -0.7$, coinciding with the ground states of the Schwinger Hamiltonian Eq. (1) for $m \rightarrow \pm\infty$. On this initial state, three alternating layers of evolution with an entangling Hamiltonian, followed by Z rotations on each qubit, are applied. The entangling Hamiltonian contains long-range XX couplings and a uniform effective magnetic field, and is given by

$$\hat{H}_E = J \sum_{j=1}^{N-1} \sum_{k=j+1}^N \frac{1}{|j-k|^\alpha} \hat{X}_j \hat{X}_k + B \sum_{j=1}^N \hat{Z}_j. \quad (7)$$

We choose $\alpha = 1$, $J = 1$, and $B = 10$ to approximate the trapped-ion experimental setup [27]. Evolution with this Hamiltonian preserves the symmetries of the lattice Schwinger model to first order terms in J/B .

Only half of the parameters in each single-qubit rotation layer are independent, as required by the symmetries, giving $\varphi_j = -\varphi_{N+1-j}$ for $j \in \{N/2 + 1, \dots, N\}$. In total, the variational circuit has 15 independent parameters for $N = 8$ lattice sites, which are initialized to zero at the start of each optimization. As a simple noise model, after each entangling layer and each single-qubit rotation layer, a depolarizing channel with $\lambda = 0.001$ is applied to each qubit (Extended Data Fig. 1a).

To optimize the variational parameters, the energy is estimated by taking samples in each of the three bases $Z^{\otimes N}$, $X^{\otimes N}$, and $Y^{\otimes N}$. The SPSA hyperparameter values are chosen by inspecting the variance and approximate gradient at the beginning of the optimization [48]. The exact values are listed in the Supplementary Information.

As input to NQST, almost-diagonal samples are taken in each of the following $2N - 1$ Pauli bases: the all- Z basis, the $(N - 1)$ bases with XX at a pair of neighbouring sites (with Z elsewhere), and the $(N - 1)$ bases with YY at a pair of neighbouring sites (with Z elsewhere). Note that for the Hamiltonian given by Eq. (1), the samples provide an estimation of the energy.

The results of the scaling study shown in Fig. 3e and Fig. 3f use a modified VQE implementation for computational efficiency. Instead of evolving the circuit using the entangling Hamiltonian, we use an entangling layer \mathcal{O}_N comprising two layers of two-qubit gates simulated without noise, as depicted in Extended Data Fig. 1b. The entangling layer was chosen to exactly preserve the symmetries of the lattice Schwinger model, while being easier to simulate numerically than evolution with \hat{H}_E . Note that, since it is composed of nearest-neighbour gates, it is also suited for superconducting quantum

hardware, especially to capacitively coupled, flux-tunable transmon qubits, where the interaction $XX + YY$ can be easily implemented [49]. For the scaling study, 1024 samples are taken in each basis to estimate the energy during SPSA optimization. The hyperparameter A of SPSA is increased to 20 and the other parameters are left unchanged.

ACKNOWLEDGEMENTS

E. R. B., F. H., B. K., and P. R. thank 1QBit for financial support. During part of this work, E. R. B. and F. H. were students at the Perimeter Institute and the University of Waterloo and received funding through Mitacs, and F. H. was supported through a Vanier Canada Graduate Scholarship. Research at the Perimeter Institute is supported in part by the Government of Canada through the Department of Innovation, Science and Economic Development and by the Province of Ontario through the Ministry of Colleges and Universities. E. R. B. was also supported with a scholarship through the Perimeter Scholars International program. P. R. thanks the financial support of Mike and Ophelia Lazaridis, and Innovation, Science and Economic Development Canada. J. C. acknowledges support from the Natural Sciences and Engineering Research Council, a Canada Research Chair, the Shared Hierarchical Academic Research Computing Network, Compute Canada, a Google Quantum Research Award, and the Canadian Institute for Advanced Research (CIFAR) AI chair program. Resources used by J. C. in preparing this research were provided, in part, by the Province of Ontario, the Government of Canada through CIFAR, and companies sponsoring the Vector Institute (www.vectorinstitute.ai/#partners). P. R. thanks Christine Muschik for useful conversations. The authors thank Marko Bucyk for carefully reviewing and editing the manuscript.

AUTHOR CONTRIBUTIONS

E. R. B. and F. H. made equal contributions. They developed the codebase for all studies, performed numerical experiments, and analyzed the results. E. R. B. performed experiments using the IBM quantum processor. E. R. B. and F. H. focused on the quantum chemistry and the lattice Schwinger model case studies, respectively. All authors contributed to ideation and dissemination. J. C. and P. R. contributed to the theoretical foundations and design of the method.

DATA AVAILABILITY

The experimental and numerical quantum simulation measurement data are available from Fig. 2 for H_2 , LiH as well as the measurement data used in Fig. 3a through

Fig. 3d for the 8 site lattice Schwinger model at <https://github.com/1QB-Information-Technologies/NEM> (see Zenodo repository [50]).

CODE AVAILABILITY STATEMENT

The numerical implementation of neural error mitigation as well as the code used to numeri-

cally implement the quantum simulations studied in the manuscript can be found at <https://github.com/1QB-Information-Technologies/NEM> (see Zenodo repository [50]).

COMPETING INTERESTS STATEMENT

The authors declare no completing interests.

-
- [1] Feynman, R. P. Simulating physics with computers. *Int. J. Theor. Phys.* **21** (1982).
- [2] Bennett, C. H. Logical reversibility of computation. *IBM Journal of Research and Development* **17**, 525–532 (1973).
- [3] Benioff, P. The computer as a physical system: A microscopic quantum mechanical Hamiltonian model of computers as represented by Turing machines. *J. Stat. Phys.* **22**, 563–591 (1980).
- [4] Manin, Y. *Computable and Noncomputable* (in Russian) (Sovetskoye Radio, Moscow, 1980).
- [5] Preskill, J. Simulating quantum field theory with a quantum computer. *arXiv:1811.10085* (2018).
- [6] Cao, Y. *et al.* Quantum chemistry in the age of quantum computing. *Chem. Rev.* **119**, 10856–10915 (2019).
- [7] McArdle, S., Endo, S., Aspuru-Guzik, A., Benjamin, S. C. & Yuan, X. Quantum computational chemistry. *Rev. Mod. Phys.* **92**, 015003 (2020).
- [8] Bauer, B., Bravyi, S., Motta, M. & Kin-Lic Chan, G. Quantum algorithms for quantum chemistry and quantum materials science. *Chem. Rev.* **120**, 12685–12717 (2020).
- [9] Aspuru-Guzik, A., Dutoi, A. D., Love, P. J. & Head-Gordon, M. Simulated quantum computation of molecular energies. *Science* **309**, 1704–1707 (2005).
- [10] Bharti, K. *et al.* Noisy intermediate-scale quantum (nisq) algorithms. *arXiv preprint arXiv:2101.08448* (2021).
- [11] Cerezo, M. *et al.* Variational quantum algorithms. *Nature Reviews Physics* **3**, 625–644 (2021).
- [12] Peruzzo, A. *et al.* A variational eigenvalue solver on a photonic quantum processor. *Nat. Commun.* **5**, 1–7 (2014).
- [13] Endo, S., Cai, Z., Benjamin, S. C. & Yuan, X. Hybrid quantum-classical algorithms and quantum error mitigation. *J. Phys. Soc. Jpn.* **90**, 032001 (2021).
- [14] Roffe, J. Quantum error correction: An introductory guide. *Contemp. Phys.* **60**, 226–245 (2019).
- [15] Dunjko, V. & Briegel, H. J. Machine learning & artificial intelligence in the quantum domain: A review of recent progress. *Reports on Progress in Physics* **81**, 074001 (2018).
- [16] Carrasquilla, J. Machine learning for quantum matter. *Advances in Physics: X* **5**, 1797528 (2020).
- [17] Torlai, G. *et al.* Neural-network quantum state tomography. *Nat. Phys.* **14**, 447–450 (2018).
- [18] Becca, F. & Sorella, S. *Quantum Monte Carlo Approaches for Correlated Systems* (Cambridge University Press, 2017).
- [19] Vaswani, A. *et al.* Attention is all you need. *arXiv:1706.03762* (2017).
- [20] Cai, Z. Multi-exponential error extrapolation and combining error mitigation techniques for NISQ applications. *arXiv:2007.01265* (2020).
- [21] Torlai, G. *et al.* Integrating neural networks with a quantum simulator for state reconstruction. *Phys. Rev. Lett.* **123**, 230504 (2019).
- [22] Song, C. *et al.* Quantum computation with universal error mitigation on a superconducting quantum processor. *Sci. Adv.* **5** (2019).
- [23] Sun, J. *et al.* Mitigating realistic noise in practical noisy intermediate-scale quantum devices. *arXiv:2001.04891* (2020).
- [24] Torlai, G., Mazzola, G., Carleo, G. & Mezzacapo, A. Precise measurement of quantum observables with neural-network estimators. *Phys. Rev. Research* **2**, 022060 (2020).
- [25] Assaraf, R. & Caffarel, M. Zero-variance principle for Monte Carlo algorithms. *Phys. Rev. Lett.* **83**, 4682 (1999).
- [26] Kandala, A. *et al.* Hardware-efficient variational quantum eigensolver for small molecules and quantum magnets. *Nature* **549**, 242–246 (2017).
- [27] Kokail, C. *et al.* Self-verifying variational quantum simulation of lattice models. *Nature* **569**, 355–360 (2019).
- [28] Klicco, N. *et al.* Quantum-classical computation of Schwinger model dynamics using quantum computers. *Phys. Rev. A* **98**, 032331 (2018).
- [29] Martinez, E. A. *et al.* Real-time dynamics of lattice gauge theories with a few-qubit quantum computer. *Nature* **534**, 516–519 (2016).
- [30] Borzenkova, O. *et al.* Variational simulation of Schwinger’s Hamiltonian with polarisation qubits. *arXiv:2009.09551* (2020).
- [31] Brydges, T., Elben, A., Jurcevic, P. Vermersch, B., Maier, C., Lanyon, Ben P., Zoller, P., Blatt, R., & Roos, C.F., Probing Renyi entanglement entropy via randomized measurements. *Science* **364**, 260–263 (2019).
- [32] Islam, R., Ma, R., Preiss, P. M. Eric Tai, M., Lukin, A., Rispoli, M., & Greiner, M., Measuring entanglement entropy in a quantum many-body system. *Nature* **528**, 77–83 (2015).
- [33] Huembeli, P. & Dauphin, A. Characterizing the loss landscape of variational quantum circuits. *Quantum Sci. Technol.* **6**, 025011 (2021).
- [34] Park, C.-Y. & Kastoryano, M. J. Geometry of learning neural quantum states. *Phys. Rev. Research* **2**, 023232 (2020).
- [35] Bukov, M., Schmitt, M. & Dupont, M. Learning the ground state of a non-stoquastic quantum Hamiltonian in a rugged neural-network landscape. *arXiv:2011.11214*

- (2020).
- [36] Hochreiter, S. & Schmidhuber, J. Long short-term memory. *Neural Comput.* **9**, 1735–1780 (1997).
 - [37] Hibat-Allah, M., Ganahl, M., Hayward, L. E., Melko, R. G. & Carrasquilla, J. Recurrent neural-network wavefunctions. *Phys. Rev. Research* **2**, 023358 (2020).
 - [38] Sharir, O., Levine, Y., Wies, N., Carleo, G. & Shashua, A. Deep autoregressive models for the efficient variational simulation of many-body quantum systems. *Phys. Rev. Lett.* **124**, 020503 (2020).
 - [39] Carrasquilla, J. *et al.* Probabilistic simulation of quantum circuits with the Transformer. *arXiv:1912.11052* (2019).
 - [40] Kingma, D. P. & Ba, J. Adam: A method for stochastic optimization. *arXiv:1412.6980* (2014).
 - [41] Carleo, G. & Troyer, M. Solving the quantum many-body problem with artificial neural networks. *Science* **355**, 602–606 (2017).
 - [42] Choo, K., Mezzacapo, A. & Carleo, G. Fermionic neural-network states for ab-initio electronic structure. *Nat. Commun.* **11**, 1–7 (2020).
 - [43] Otis, L. & Neuscammann, E. Complementary first and second derivative methods for ansatz optimization in variational Monte Carlo. *Phys. Chem. Chem. Phys.* **21**, 14491–14510 (2019).
 - [44] Bravyi, S. B. & Kitaev, A. Y. Fermionic quantum computation. *Annals of Physics* **298**, 210–226 (2002).
 - [45] Seeley, J. T., Richard, M. J. & Love, P. J. The Bravyi–Kitaev transformation for quantum computation of electronic structure. *J. Chem. Phys.* **137**, 224109 (2012).
 - [46] Bravyi, S., Gambetta, J. M., Mezzacapo, A. & Temme, K. Tapering off qubits to simulate fermionic Hamiltonians. *arXiv:1701.08213* (2017).
 - [47] Abraham, H. *et al.* Qiskit: An open-source framework for quantum computing, 2019. <https://qiskit.org> (2019).
 - [48] Spall, J. C. Implementation of the simultaneous perturbation algorithm for stochastic optimization. *IEEE Trans. Aerosp. Electron. Syst.* **34**, 817–823 (1998).
 - [49] Krantz, P. *et al.* A quantum engineer’s guide to superconducting qubits. *Appl. Phys. Rev.* **6**, 021318 (2019).
 - [50] Bennewitz, E. R., Hopfmueller, F., Kulchytskyy, B., Carrasquilla, J. & Ronagh, P. 1QB-Information-Technologies/NEM: 1QB-Information-Technologies/Neural Error Mitigation (2022). URL <https://doi.org/10.5281/zenodo.6466405>.

Supplementary Information: Neural Error Mitigation of Near-Term Quantum Simulations

I. DETAILS OF THE TRANSFORMER NEURAL QUANTUM STATE

We use the Transformer [1] neural network architecture to represent neural quantum states. The Transformer can be applied to represent probability distributions and other functions over one-dimensional sequences of discrete data. At its core is self-attention, a mechanism that learns correlations by assigning attention weights to each pair of positions (i.e., how much the output at one position of a given sequence should depend on the input at another position). Each layer of the Transformer contains a self-attention component, which, in turn, consists of several independent so-called self-attention heads. Within a self-attention component, each of these heads have independent parameters, and act on the layer inputs independently in parallel. The output of the self-attention component is the concatenation of the outputs of each head. In each head, for every pair of positions in the sequence, the attention weight is computed from the inputs at those positions, using key and query vectors. The output at each position is a sum, weighted by the attention weights, of the value vectors at all positions. To improve the representation power of the model, the self-attention components alternate with linear layers, which act on each position individually. To ensure the stability of the model, skip-connections and layer normalization are employed within each layer. A single Transformer layer with all of its components is depicted in Fig. S1.

Recall from the Methods section of the main manuscript that the neural quantum state maps a bitstring $s \in \{0, 1\}^N$ to a tuple $(p(s), \varphi(s))$, with $\langle s|\psi\rangle = \sqrt{p(s)}e^{i\varphi(s)}$, where N is the number of qubits. The computational cost of calculating $\langle s|\psi\rangle$ for a single computational basis state s is quadratic in the number of qubits, and alternative versions of the Transformer architecture improve this cost to being linear (e.g., [2]).

More specifically, the outputs $p(s)$ and $\varphi(s)$ are obtained from the bitstring s as follows. The bitstring s is extended to $\tilde{s} = (0, s)$ by prefixing a zero bit. Each bit \tilde{s}_n of the input is encoded into a D -dimensional representation space using a learned embedding, yielding the encoded bit $e_{nd}^{(0)}$ with $n \in \{0, \dots, N\}$ and $d \in \{1, \dots, D\}$. Each index n is encoded using a learned positional encoding, yielding the encoded index f_{nd} . The encoded input is processed using K identical layers. Each layer consists of a masked multi-head self-attention mechanism [1], with H heads, followed by a linear layer, with skip-connections and layer normalization. The weights of the attention matrices and the linear layer are shared between the positions n , but not between the layers k .

The parameters of a single layer k are:

1. The query, key, and value matrices $Q_{hid}^{(k)}$, $K_{hid}^{(k)}$, and $V_{hid}^{(k)}$. The index $h \in \{1, \dots, H\}$ labels the self-attention heads. The index $i \in \{1, \dots, D/H\}$ runs over a representation space of dimension D/H , where we require that D/H be an integer. As before, we have $d \in \{1, \dots, D\}$.
2. A matrix to process the output of the self-attention heads, $O_{de}^{(k)}$, with $d, e \in \{1, \dots, D\}$.
3. A weight matrix and a bias vector of the linear layer, $W_{de}^{(k)}$ and $b_d^{(k)}$, with $d, e \in \{1, \dots, D\}$.

The self-attention component acts as follows:

1. We denote the input to the component by $i_{SA,nd}^{(k)}$, where $n \in \{0, \dots, N\}$ and $d \in \{1, \dots, D\}$. Query, key, and value vectors are computed as $q_{nhi}^{(k)} = \sum_d Q_{hid}^{(k),i(k)} i_{SA,nd}^{(k)}$, $k_{nhi}^{(k)} = \sum_d K_{hid}^{(k),i(k)} i_{SA,nd}^{(k)}$, and $v_{nhi}^{(k)} = \sum_d V_{hid}^{(k),i(k)} i_{SA,nd}^{(k)}$.
2. Attention weights are computed as follows. Compute the attention scores $s_{nmh}^{(k)} = \sum_i q_{nhi}^{(k)} k_{mhi}^{(k)}$. Mask the attention scores by setting $s_{nmh}^{(k)} = -\infty$ whenever $m < n$. Compute the attention weights using the softmax

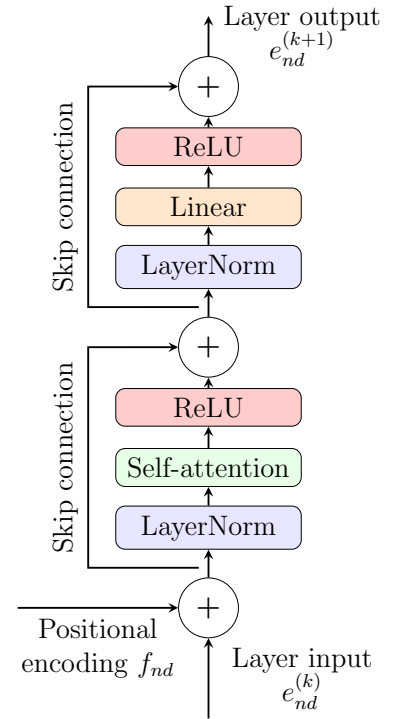


FIG. S1: **Illustration of a Transformer layer** | The Transformer consists of several layers acting in sequence. The central components of a Transformer layer are the self-attention block and linear layer. To enable a position-aware output, at each layer a positional encoding of the index n is added to the input. To enhance stability, a skip connection and layer normalization are employed.

function given by

$$w_{nmh}^{(k)} = \frac{\exp(s_{nmh}^{(k)})}{\sum_{m'} \exp(s_{nm'h}^{(k)})}. \quad (\text{S1})$$

The masking ensures that $w_{nmh}^{(k)} = 0$ whenever $m < n$.

3. The output of each attention head is $a_{nhi}^{(k)} = \sum_m w_{nmh}^{(k)} v_{mhi}^{(k)}$. At each position n , concatenate the output of the attention heads; that is, reshape the indices h and i into one index d , giving $a_{nd}^{(k)}$.
4. The output of the self-attention component is $o_{\text{SA},nd}^{(k)} = \sum_e O_{de}^{(k)} a_{ne}^{(k)}$. Due to the masking, the output at position n depends on the inputs only at positions $m \leq n$. We write the action of the entire self-attention component more abstractly as $A^{(k)}$, that is, $o_{\text{SA}}^{(k)} = A^{(k)}(i_{\text{SA}}^{(k)})$.

The linear component acts on an input $i_{\text{L},nd}^{(k)}$ as $o_{\text{L},nd}^{(k)} = \sum_e W_{de}^{(k)} i_{\text{L},nd}^{(k)} + b_d^{(k)}$, which we write more abstractly as $o_{\text{L}}^{(k)} = L^{(k)}(i_{\text{L}}^{(k)})$. Both components are wrapped with a skip-connection, layer normalization [3], and a ReLU activation function. The output of the wrapped self-attention component $A^{(k)}$, acting on an input $i_{nd}^{(k)}$, is

$$a^{(k)} = G(A^{(k)}, i^{(k)}) = i^{(k)} + \text{ReLU}\left(A^{(k)}(\text{LayerNorm}(i^{(k)}))\right), \quad (\text{S2})$$

where $\text{ReLU}(x) = \max(x, 0)$ is the ReLU activation function acting component-wise, and layer normalization is applied on the last dimension of $i_{nd}^{(k)}$. We have introduced the notation G for the wrapping. The linear component $L^{(k)}$ is wrapped in the same manner, giving $e^{(k)} = G(L^{(k)}, a^{(k)})$. In sum, the action of the entire Transformer layer is as follows:

1. The input to the k -th layer is $i_{nd}^{(k)} = e_{nd}^{(k-1)} + f_{nd}$.
2. The wrapped self-attention component is applied to give $a^{(k)} = G(A^{(k)}, i^{(k)})$.
3. The wrapped linear layer is applied to give $e^{(k)} = G(L^{(k)}, a^{(k)})$.

After the final Transformer layer, the outputs of the neural quantum state are obtained from the final representation $e_{nh}^{(K)}$ as follows. Scalar-valued logits ℓ_n are obtained from $e_{nh}^{(K)}$ using a linear layer, with weights shared among different positions n . The logits are used to obtain conditional probabilities according to

$$\begin{aligned} p(s_n = 1 | s_1, \dots, s_{n-1}) &= \sigma(\ell_{n-1}) \quad \text{and} \\ p(s_n = 0 | s_1, \dots, s_{n-1}) &= 1 - p(s_n = 1 | s_1, \dots, s_{n-1}) = \sigma(-\ell_{n-1}), \quad \text{where } n \in \{1, \dots, N\}, \end{aligned} \quad (\text{S3})$$

and $\sigma(\ell_{n-1}) = \frac{1}{1 + e^{-\ell_{n-1}}}$ is the logistic sigmoid function. The conditional probabilities give $p(s)$ via the conditional probability chain rule

$$p(s) = \prod_{n=1}^N p(s_n | s_1, \dots, s_{n-1}), \quad (\text{S4})$$

where $p(s)$ is an automatically normalized probability distribution.

The factorization of the probabilities $p(s)$, along with the fact that the neural network output at position n depends only on the positions $m \leq n$, may be leveraged to efficiently draw unbiased samples from the probability distribution p . To do so, we proceed a single bit at a time. First, we compute $p(s_1 | s_0 = 0)$, and sample the bit s_1 from the resulting probability distribution. We then compute $p(s_2 | s_0, s_1)$ and sample the bit s_2 from it, and so on, until all bits have been sampled. The sampling is needed when training the NQS using VMC, as explained in the next section.

The phase $\varphi(s)$ is obtained by forming a vector $E^{(K)} = (e_0^{(K)}, \dots, e_N^{(K)})$ by concatenating the final representations, and projecting $E^{(K)}$ to a scalar value using a linear layer. Our Transformer is implemented in PyTorch [4], and is partially inspired by aspects of the implementations in Refs. [5, 6].

II. VMC TRAINING AND REGULARIZATION

In the final step of NEM described in the Methods section in the main manuscript, the neural quantum state is trained using VMC. We add the regularizer

$$L_{\text{reg}} = -\epsilon_{\text{reg}} \sum_{s \in \{0,1\}^N} \left| \langle s | \psi_{\vec{\lambda}} \rangle \right| \quad (\text{S5})$$

to the loss function, where ϵ_{reg} is a coefficient that is decreased over the course of training. The regularizer maximizes the L_1 -norm of the wavefunction, thereby discouraging sparsity in the early stages of training. For ground states that are known to overlap greatly with one or a few ground states, this regularization technique encourages the NQS to capture subdominant amplitudes rather than collapsing onto the dominant contributions (e.g., the Hartree–Fock states, or the lattice Schwinger ground states at $m \rightarrow \pm\infty$) early in the training process.

As with the energy, the regularizer and its gradient with respect to the parameters $\vec{\lambda}$ of the neural quantum state $|\psi_{\vec{\lambda}}\rangle$ need to be estimated from samples using the Monte Carlo method, giving the expressions

$$\begin{aligned} L_{\text{reg}} &= -\epsilon_{\text{reg}} \mathbb{E}_{s \sim p_{\vec{\lambda}}} \left[\left| \langle s | \psi_{\vec{\lambda}} \rangle \right|^{-1} \right] \approx -\epsilon_{\text{reg}} \frac{1}{b} \sum_{i=1}^b \left| \langle s^i | \psi_{\vec{\lambda}} \rangle \right|^{-1} \quad \text{and} \\ \nabla_{\theta} L_{\text{reg}} &= -\epsilon_{\text{reg}} \mathbb{E}_{s \sim p_{\vec{\lambda}}} \left[\left| \langle s | \psi_{\vec{\lambda}} \rangle \right|^{-1} \nabla_{\vec{\lambda}} \Re(\ln \langle s | \psi_{\vec{\lambda}} \rangle) \right] \approx -\epsilon_{\text{reg}} \frac{1}{b} \sum_{i=1}^b \left[\left| \langle s^i | \psi_{\vec{\lambda}} \rangle \right|^{-1} \nabla_{\vec{\lambda}} \Re(\ln \langle s^i | \psi_{\vec{\lambda}} \rangle) \right]. \end{aligned} \quad (\text{S6})$$

Here, \Re denotes the real part, the expectation values are taken over $p_{\vec{\lambda}}(s) = |\langle s | \psi_{\vec{\lambda}} \rangle|^2$, s^i are samples from the same distribution, and b is the batch size used in VMC.

The regularizer’s gradient is added to the energy’s gradient at every iteration. For completeness, we reproduce the VMC algorithm here:

1. Draw b samples $\{s^1, \dots, s^b\}$ from $p_{\vec{\lambda}}(s) = |\langle s | \psi_{\vec{\lambda}} \rangle|^2$.
2. Compute the local Hamiltonians for all $s^i \in \{s^1, \dots, s^b\}$:

$$H_{\text{loc}}(s^i) = \sum_{\substack{t \in \{0,1\}^N \\ \langle s^i | \hat{H} | t \rangle \neq 0}} \frac{\langle s^i | \hat{H} | t \rangle \langle t | \psi_{\vec{\lambda}} \rangle}{\langle s^i | \psi_{\vec{\lambda}} \rangle} \quad (\text{S7})$$

3. Estimate the energy and its gradient with respect to the parameters $\vec{\lambda}$ of $|\psi_{\vec{\lambda}}\rangle$ using

$$\begin{aligned} E &\approx \frac{1}{b} \Re \left(\sum_{i=1}^b H_{\text{loc}}(s^i) \right) \quad \text{and} \\ \nabla_{\theta} E &\approx \frac{2}{b} \Re \left[\sum_{i=1}^b (E_{\text{loc}}(s^i) - E) \nabla_{\theta} \ln \langle s_i | \psi_{\vec{\lambda}} \rangle \right], \end{aligned} \quad (\text{S8})$$

where $\ln \langle s | \psi_{\vec{\lambda}} \rangle = \ln \sqrt{p(s)} + i\varphi(s)$ in terms of the neural network’s outputs.

4. Estimate the regularizer and its gradient.
5. Add the energy’s gradient and the regularizer’s gradient, and update the parameters using the Adam optimizer.

III. EXPERIMENTAL VQE RESULTS FOR LiH

We can analyze the quality of the variational procedure implemented on the five-qubit IBMQ-Rome device by looking at the energy optimization curves of the experimental results of VQE implemented for various bond lengths of LiH (see Fig. S2). Generally, the optimization curves show that the experimental VQE procedure performs as

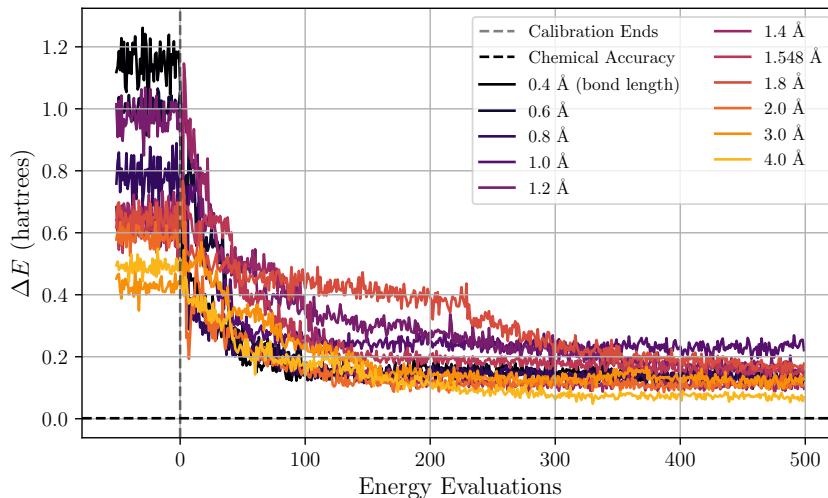


FIG. S2: **Experimental VQE energy optimization curves** | Energy evaluations during SPSA optimization for LiH ground states at different bond lengths using a five-qubit superconducting quantum computer. In order to compare optimization curves for all bond lengths, we plot the energy difference to the ground state as a function of SPSA energy evaluations. Before optimization, the energy is estimated 25 times and used to calibrate the initial step size of the algorithm. These energy values are reported to the left of the vertical dashed line. During each SPSA iteration, the energy is estimated using 25 measurement bases with 1024 measurements per measurement basis. The parameters $\vec{\theta}$ are updated 250 times, resulting in 500 energy evaluations. Note that three bond lengths show incomplete convergence by the end of the optimization process, with one bond length (1.8), still decreasing. Although VQE does not reach convergence for all bond lengths, neural error mitigation is able to improve the results up to chemical accuracy, with low infidelity, as shown in the top row of Fig. 2 in the main manuscript.

expected, with energy optimization curves decreasing and converging to low energy estimates. However, we also see that the simulation is unable to reach high-accuracy energy estimates, $\Delta E \lesssim 10^{-3}$. This is due to the effects of noise on, and limitations of, the variational quantum circuit [7]. Despite these errors, neural error mitigation is able to extend all experimental results up to chemical accuracy, with low infidelities. We refer the reader to Table S1 for the specific hyperparameters used in implementing VQE and NEM.

IV. QUANTUM STATE RECONSTRUCTION

An important feature of NEM is the ability to analyze the quality of the reconstructed neural quantum state at various stages of the NEM algorithm. Since NEM employs NQS at the core of its construction, we have direct access to the reconstructed quantum state through the probability, $p(s)$, and phase, $\phi(s)$, distributions given by, $p(s) = |\langle s|\psi\rangle|^2$ and $\psi(s) = \arg(\langle s|\psi\rangle)$. We analyze the reconstructed quantum state obtained after NQST as well as the final NEM procedure for both of the systems studied in this paper, and compare the probability distributions modelled by the neural quantum states to the VQE result. The VQE state is given by a density matrix ρ , because VQE is numerically simulated using a density matrix simulator. The probability amplitudes of ρ are given by $p(s) = \text{Tr}(\rho |s\rangle\langle s|)$. Since we simulate VQE with noise, the VQE density matrix ρ describes a mixed state instead of a pure state. For mixed states, the phase is not well-defined, and therefore not reported in Fig. S3 and Fig. S4.

In Fig. S3, we show the quantum states estimated at each stage of our process for the LiH ground states at a bond length of $l = 1.4$ Å, prepared both experimentally (Fig. S3a) and numerically (Fig. S3b). We see that, for numerical results, where we have access to the VQE quantum state, neural quantum state tomography accurately reconstructs the optimized VQE state using the chosen measurement bases. For the experimental results, where we do not have access to the final VQE quantum state, the neural quantum state trained using neural quantum state tomography acts as an estimator of the final state expressed by the quantum device. At this stage, the neural quantum state trained using NQST has not captured the exact ground state’s phase structure and inaccurately represents some of the non-dominant computational basis states. After the NEM algorithm has been completed, the final NEM state achieves accurate representations of both the probability distribution and phase for the computational basis states whose exact probabilities are greater than 10^{-5} (or greater than 10^{-4} for experimental results). In the process of improving the energy estimation achieved by VQE, NEM reconstructs and improves the ground-state wavefunction itself. From another perspective, the classical ansatz trained through this process extends the “lifetime” of the quantum simulation [8], allowing for its use in future work, without having to repeat the experiment.

Figure S4 shows a representation of the VQE state, as well as the neural quantum state after applying NQST and after having completed NEM for the lattice Schwinger model. The phase structures of the lattice Schwinger

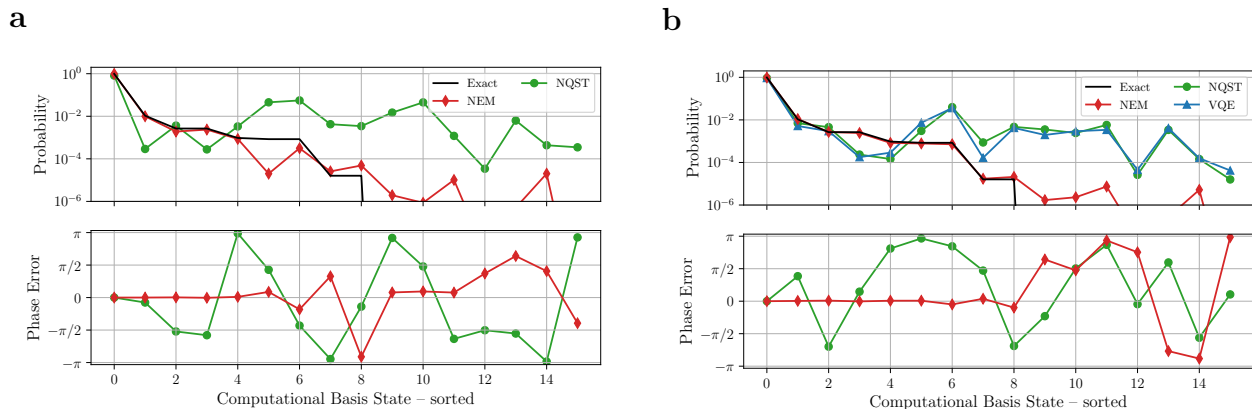


FIG. S3: **Quantum states at each step in the neural error mitigation algorithm for LiH** | The quantum states obtained by VQE (blue triangles), neural quantum state tomography (green circles), and neural error mitigation (red diamonds) for the LiH ground state at a bond length of $l = 1.4 \text{ \AA}$. In contrast to the neural quantum state, the VQE state is given by a density matrix representing a mixed state because VQE is simulated using a noisy density matrix simulator. Whereas the probability distribution is given by $p(s) = \text{Tr}(\rho|s\rangle\langle s|)$, the phase for a mixed state is not well-defined, and therefore not reported. In each subfigure, the top panel shows the probabilities for the NQS given by $p(s) = |\langle s|\psi\rangle|^2$ for each computational basis state $|s\rangle$. Computational basis states are sorted according to these probability amplitudes. The bottom panel shows the phase error of the NQS relative to the ground state given by $\arg(\langle s|\psi\rangle) - \arg(\langle s|\psi_g\rangle)$, where the global phase is fixed to a phase error of zero for the computational basis state that has the largest ground state probability. Neural error mitigation applied to an experimentally prepared VQE result is shown on the left (a), and NEM applied to a numerically simulated VQE result is shown on the right (b). Under our qubit encoding for the electronic structure problem, the Hartree-Fock state is mapped to a computational basis state and constitutes the dominant contribution to the exact ground state corresponding to the 0-th state on the horizontal axis. This results in an exact probability distribution that has a sharp peak, as shown traced by the black line. We see that the neural quantum states trained using NQST approximately reconstruct the VQE quantum state's probability distribution, for the numerically simulated results. In addition, the final probability distribution represented by the NEM states very accurately represents the basis states with exact probabilities greater than 10^{-5} for numerical simulations and greater than 10^{-4} for our experimental results. The phase errors are shown in the bottom panel, where we see that the final NEM quantum state accurately reconstructs the phase for computational basis states with probabilities greater than 10^{-5} for numerical simulations and greater than 10^{-4} for our experimental results.

ground states follow a sign rule and have real amplitudes. Although possible, we do not enforce the sign rule or any symmetries in our neural quantum states in order to show the general applicability of NEM. While the fidelity of the NQST state with respect to the ground state is only 0.71, the errors in the complex phases that correspond to the computational basis states with non-zero amplitudes are relatively small, and mostly confined to the range $[-\frac{\pi}{2}, \frac{\pi}{2}]$. Given that converging to an accurate phase structure is one of the main difficulties encountered in training a neural network using VMC [9], the NQST state may provide a good starting point from which it could be easy for the VMC algorithm to converge to a good approximation of the ground state. After the NEM algorithm has completed, the final NEM state achieves an accurate representation of both the probability distribution and the phases of the lattice Schwinger ground state, specifically for the computational basis states whose exact probabilities are greater than 10^{-5} .

V. COMPARISON OF NEM TO VMC

The key observation outlined in this paper is that NQST and VMC can be combined to form a post-processing error-mitigation strategy for ground-state preparation when the two procedures are conducted using a common neural network ansatz. In addition to analyzing how well NEM improves the results obtained from noisy quantum simulations, it is also useful to compare NEM to its classical counterpart: training a neural quantum state using only the variational Monte Carlo algorithm, hereafter referred to as *standalone* VMC. We compare the performance of both methods as a function of VMC batch size, which is the number of samples used in estimating the gradient and updating the neural network's parameters during VMC (see Section II). Given that we fix the total number of iterations used in training, the batch size is indicative of the classical computational resources required. Note that increasing the batch size decreases the variance of the energy's gradient estimate. For larger systems, a large batch size is often required in order to reach chemical accuracy, which imposes a bottleneck on the possible applications of VMC [10]. Another way to increase the amount of classical computational resources, which may exhibit different scaling, would be to increase the number of iterations at a fixed batch size.

In Fig. S5 we compare the energy error and infidelity of NEM performed on the experimental VQE result and standalone VMC, for the LiH molecule at a bond length of $l = 1.4 \text{ \AA}$ (the same experimental VQE data is presented in the top row of Fig. 2 in the main manuscript). For NEM, we fix the outcome of the first stage of NEM (i.e., the neural quantum state trained via NQST) and then train the VMC component of NEM using different batch sizes to

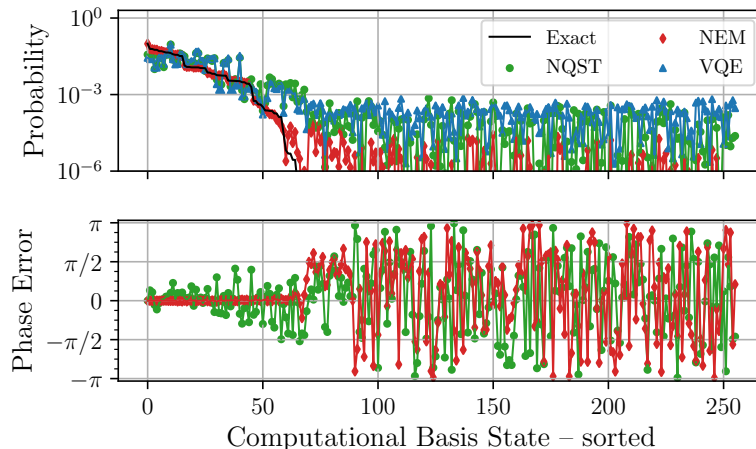


FIG. S4: **Quantum states at each step of the neural error mitigation algorithm for the $N = 8$ lattice Schwinger model** | The quantum states obtained by VQE (blue triangles), by NQST (green circles), and after completion of NEM (red diamonds) are shown, for the lattice Schwinger model at $m = -0.7$. Similar to Fig. S3, the top panel shows the probabilities of each basis state sorted according to their probability amplitudes, and the bottom panel shows the phase errors with respect to the exact ground-state phase. In contrast to the NQS results, the VQE state is given by a mixed-state density matrix. Therefore, we report the VQE probability distribution but not the phase. Due to the symmetries present in the lattice Schwinger ground state, many computational basis state amplitudes are zero in the exact ground-state probability distribution (solid black line). While the probabilities of the VQE state somewhat follow the ground state, the VQE state overestimates many of the computational basis states' probabilities that do not contribute to the exact ground state. This is explained by the effects of noise and because the quantum circuit employed only approximately preserves the symmetries of the model. We can see that NQST successfully reconstructs the VQE state, accurately modelling the probability distribution for the computational basis states that contribute to the exact ground state. Additionally, NQST provides an estimate of the phase, showing a phase error confined mostly to the range $[-\pi/2, \pi/2]$ for the computational basis states that make non-zero contributions to the exact ground state. At the end of NEM, the final probability distribution represented by the NEM state accurately represents the probabilities and phases of the computational basis states that have exact probabilities greater than 10^{-5} .

investigate how the energy error and infidelity of the final NEM state scales. The results show that NEM performed using the experimental results provides an advantage over using only VMC. NEM achieves chemical accuracy using a lower batch size than VMC. In addition we note that NEM requires a smaller regularizer compared to conducting the training using only VMC. Note that the ground states of LiH, a molecular system that can be mapped to four qubits, can be feasibly solved using current classical methods.

For the lattice Schwinger model, we also study the performance of NEM and standalone VMC as a function of system size and batch size (Fig. S6). We show that while the best results for standalone VMC are comparable to the best results of NEM, standalone VMC has a lower success rate, especially for larger systems and smaller batch sizes. Conversely, NEM reliably converges to a good approximation of the ground state. We speculate that the state found by VQE, which is approximated by NQST, provides a good initialization for training using VMC, and explains the improved convergence rate of the NEM algorithm. While we expect that, for system sizes presented, hyperparameter tuning could potentially improve the results of standalone VMC, we speculate that the increased stability of NEM over standalone VMC will persist at larger system sizes.

In order to understand the advantages of using quantum resources in conjunction with classical methods, future research must be conducted to explore whether using the NEM algorithm for preparing ground states, such as those for larger systems in quantum chemistry and lattice theories, converges to classical representations of quantum states that are outside the reach of standalone VMC. This speculation stems from the fact that both NEM and standalone VMC train a neural quantum state using the VMC algorithm, with the difference being that NEM initializes the VMC algorithm using a classical representation of an experimentally prepared quantum state. One approach could be to determine whether the NEM algorithm captures features of the experimentally prepared quantum state, such as superposition and entanglement, in its initial neural quantum state representation and whether it retains these features throughout the classical training process. We also speculate that exploring the loss landscape of VMC can help to delineate the boundary between classically solvable ground-state preparation problems and those that require quantum resources. In other words, we ask whether initializing VMC using a classical representation of an experimentally prepared quantum state relaxes classical resource requirements of the VMC algorithm, such as the exponentially large amount of memory needed to describe high-fidelity ground-state representations. The work presented in this paper provides a framework for investigating the fundamental differences and potential synergy between quantum and classical information processing.

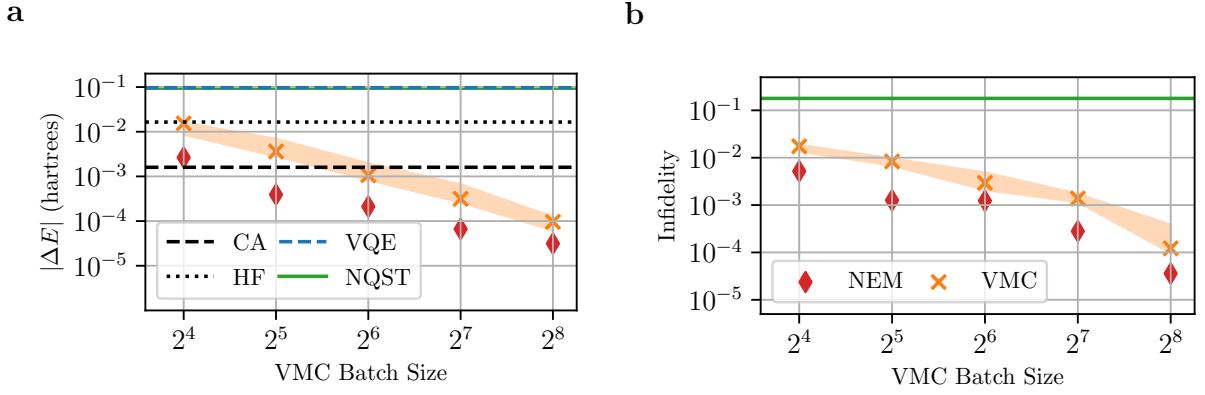


FIG. S5: **Comparison between neural error mitigation and variational Monte Carlo for quantum chemistry** | The performance of neural error mitigation (red diamonds) on experimental VQE results compared to the performance of training a neural quantum state using standalone VMC (orange crosses) is shown. Both methods are compared as a function of the VMC batch size for the LiH ground state for $l = 1.4$. Both methods are performed using a neural quantum state that has both the same architecture hyperparameter values. The median results for VMC are shown for 10 runs, and the shaded regions show the interquartile range. In (a), the chemical accuracy (CA) and Hartree–Fock (HF) energy error are reported. For LiH, NEM applied to the experimental results outperforms standalone VMC, achieving chemical accuracy at a batch size at a factor of two earlier than standalone VMC.

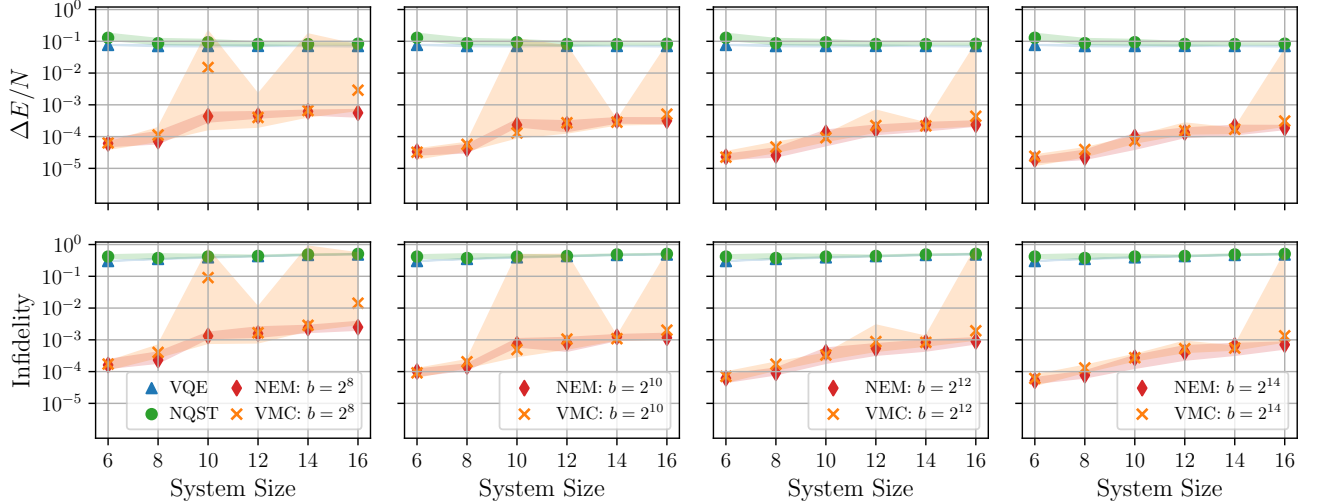


FIG. S6: **Comparison between neural error mitigation and variational Monte Carlo for the lattice Schwinger model** | Performance of standalone VMC on the lattice Schwinger model, compared to the performance of NEM, for various system sizes N and batch sizes b . While the best results achieved by standalone VMC are no worse than the best results achieved by NEM, standalone VMC does not consistently converge to a high-quality approximation of the ground state. Neural error mitigation is more stable, especially at smaller batch sizes and larger system sizes. Each panel shows the median results, and the shaded regions show the interquartile ranges. The hyperparameter values used for standalone VMC are the same as those used in the scaling analysis shown in Fig. 3e and Fig. 3f of the main manuscript, and are listed in the column “> 8 sites” of Table S1.

VI. COMPARISON OF NEM ACROSS DIFFERENT LEVELS OF NOISE IN VQE

The results presented in this paper have shown that NEM can improve estimates of ground states and ground state properties obtained from VQE on noisy devices and in noisy simulations by supplementing these noisy VQE results with classical simulation methods. However, for high levels of noise, we expect the results obtained from VQE to contain less information about the true ground state. Beyond a certain level of noise, we expect that supplementing VQE with NEM should not outperform an NQS trained using purely classical methods such as VMC. In order to determine the regime where the combination of VQE and NEM holds the promise of improvement over purely classical methods, we study the performance of NEM as a function of VQE noise levels.

We consider the eight-site Schwinger model, at the critical point $m = -0.7$, and compare the performance of NEM for VQE noise rates ranging from zero noise to complete depolarization. The VQE circuit used is the same as the results shown in Fig. 4a of the main manuscript, and has an initial state of $|01 \dots 01\rangle$. After each layer of the global entangling operation or single-qubit rotations, a depolarizing channel with a variable rate $\lambda \in [0, 1]$ is applied to each

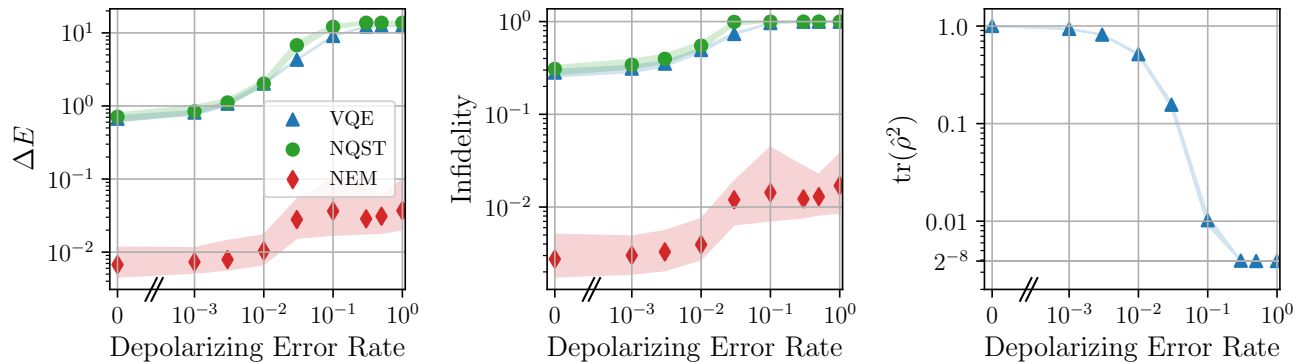


FIG. S7: **Comparison of the performance of NEM across different levels of noise in VQE** | Performance of neural error mitigation applied to VQE results for the eight-site Schwinger model at the critical mass $m = -0.7$. Single-qubit depolarizing noise gates of various noise rates λ are applied after every operation in the simulation of the VQE circuit. The NEM performance when $\lambda = 1$ can be attributed to classical resources only, since the output of VQE corresponds to a state close to the maximally mixed state. At $\lambda \leq 10^{-2}$, corresponding to a purity of $\text{tr}(\rho^2) \geq 0.82$, the results of NEM show a clear improvement over those of classical resources alone. Shown is the median over 100 runs. The shaded region represents the interquartile range.

qubit. The hyperparameters for NQST and VMC are the same as in the main manuscript.

At a depolarizing error rate of $\lambda = 1$, the VQE results are highly mixed and thus contain no information about the true ground state or its properties, as noise completely dominates the simulation. While even in the completely depolarizing simulation, NEM yields an improvement over VQE, its performance can be attributed to that of VMC which uses only classical computational resources. Thus, the results obtained when $\lambda = 1$ can be used as a benchmark for the performance of standalone VMC. The results in Fig. S7 show that at noise rates of $\lambda = 10^{-2}$ or lower, corresponding to a median purity $\text{tr}(\rho^2) \geq 0.82$ of the VQE density matrix, the energy error and infidelity of the NEM state yield a clear improvement over the NEM results when $\lambda = 1$. These results underscore the fact that NEM used in conjunction with VQE shows an improvement over a computation that uses only classical resources given that the quality of the quantum resources meets a minimum threshold for the system studied.

VII. HYPERPARAMETER VALUES

We present the hyperparameter values of our numerical studies in Table S1.

	Lattice Schwinger (8 sites)	Lattice Schwinger (> 8 sites)	H₂	LiH
Variational Quantum Eigensolver				
Iterations	200	200	250	250
Post-rotation circuits	3	3	4	25
Shots per basis	512	1024	1024	1024
<i>SPSA parameters:</i>				
a_0	0.1	0.1	calibrated [†]	calibrated
c_0	0.1	0.1	0.1	0.1
α	0.602	0.602	0.602	0.602
γ	0.101	0.101	0.101	0.101
A	10	20	0	0
Neural Quantum State				
<i>Transformer parameters:</i>				
Layers	2	2	2	2
Heads	4	4	4	4
Internal dimension	8	12	8	8
Parameter count	890	1766–2006	794	826
Neural Quantum State Tomography				
Bases	15	$2N - 1$	4	11
Samples per basis	512	512	300	500
Batch size	512	512	128	128
Learning rate	10^{-2}	10^{-3}	10^{-2}	10^{-2}
Epochs	50	30	100	100
Time (Single CPU)	< 1 minute	8 minutes (16 sites)	30 seconds	6 minutes
Variational Monte Carlo				
Iterations	400	3200	1000	1200
Batch size	512	$2^8 - 2^{14}$	256	256
Learning rate	10^{-2}	3×10^{-3} then decreased by 10 times after 1600 and 2400 iterations	10^{-2}	10^{-2}
Regularization	0.1 for 200 iterations, then 0	$25.6/(2^N)$ decreasing linearly for 1000 iterations, then 0	0.05 for 600 iterations, then 0	0.05 for 600 iterations, then 0
Time (Single CPU)	< 1 minute	6 hours (16 sites)	10 seconds	20 seconds

TABLE S1: **Hyperparameter values for neural error mitigation components** | Presented are the hyperparameter values of the neural quantum state, VQE training, neural quantum state tomography, and variational Monte Carlo for each system studied. [†]The a_0 parameter for each H₂ and LiH variational circuit is calibrated [7] in Qiskit’s VQE function.

-
- [1] Vaswani, A. *et al.* Attention is all you need. *arXiv:1706.03762* (2017).
 - [2] Wang, S. *et al.* Linformer: Self-attention with Linear Complexity. *arXiv:2006.04768* (2020).
 - [3] Ba, J. L., Kiros, J. R. & Hinton, G. E. Layer normalization. *arXiv:1607.06450* (2016).
 - [4] Paszke, A. *et al.* Pytorch: An imperative style, high-performance deep learning library. *arXiv:1912.01703* (2019).
 - [5] Dai, Z. *et al.* Transformer-xl: Attentive language models beyond a fixed-length context. *arXiv:1901.02860* (2019).
 - [6] Parisotto, E. *et al.* Stabilizing Transformers for reinforcement learning. In *International Conference on Machine Learning*, 7487–7498 (PMLR, 2020).
 - [7] Kandala, A. *et al.* Hardware-efficient variational quantum eigensolver for small molecules and quantum magnets. *Nature* **549**, 242–246 (2017).
 - [8] Torlai, G. *et al.* Neural-network quantum state tomography. *Nat. Phys.* **14**, 447–450 (2018).
 - [9] Szabó, A. & Castelnovo, C. Neural-network wavefunctions and the sign problem. *Phys. Rev. Research* **2**, 033075 (2020).
 - [10] Choo, K., Mezzacapo, A. & Carleo, G. Fermionic neural-network states for ab-initio electronic structure. *Nat. Commun.* **11**, 1–7 (2020).